sensibat

D 2.4 – REPORT ON LEVEL 2 SENSOR MORPHOLOGICAL AND ELECTROCHEMICAL CHARACTERISATION

LC-BAT-13-2020 - Sensing functionalities for smart battery cell chemistries

Deliverable No.	2.4	
Related WP	2	
Deliverable Title	Report on level 2 sensor morphological and electrochemical characterisation	
Deliverable Date	30-08-2022	
Deliverable Type	REPORT	
Dissemination level	Public (PU)	
Written By	Silvia Bodoardo (POL)	04-07-2022
	Piera Di Prima (POL)	13-07-2022
	Hossein Beydaghi (BDM)	14-08-2022
Checked by	Sebastiano Bellani (BDM)	17-08-2022
Reviewed by	Iñigo Gandiaga (IKE)	19-08-2022
	Francesco Bonaccorso (BDM)	24-08-2022
Approved by	Iñigo Gandiaga (IKE)	26-08-2022
Status	Final	26-08-2022

Summary

The deliverable D.2.4 "Report on level 2 sensor morphological and electrochemical characterisation" describes the activities related to the Task 2.4 of the WP2. It is focused on the characterisation and testing of printed sensor in form of high-conductivity graphene-based reference electrodes printed on Celgard 2500 separator, to be used for electrodes' potential monitoring and Electrochemical Impedance Spectroscopy (EIS) measurements in pouch cell battery configurations. The complete physicochemical and electrochemical characterizations reported in the present document allowed to choose the best performing sensor between LFP and LTO. The results indicated LTO as the best material to assemble full cells based on NMC cathode and graphite anode. The measurement of the voltage of each electrode during cycling the full cell is successfully demonstrated.

This deliverable and the related task do not include any deviation from the objectives and timings planned in the Grant Agreement of the SENSIBAT project.

Table of Contents

List of Figures

Figure 20. a) Scheme of the cell connections. (*Orange*: cathode; *Dark grey*; anode and the reference electrode-coated Celgard®2500; *Light grey*: uncoated separator). b) Voltage profiles for the whole cell (black line) and for the graphite anode (red line).

Figure 21. Galvanostatic cycling a) at C/10 and C/5 and b) at C/5 of Li - LTO-B 240µm - NMC622.

Figure 22. Galvanostatic cycling at C/10, C/5, C/2, 1C and C/10 of Li - LTO-B 54µm - NMC622.

Figure 23. Discharge capacity of complete cells at different C-rates.

Figure 24. Example of new sample sent by BDM to POL.

List of Tables

Abbreviations

Symbol / Abbreviation	
C	*Capacitance*
CB	*Carbon black*
CC	*Constant Current*
CV	*Cyclic Voltammetry*
DC	*Direct Current*
EC:DEC	*Ethyl Carbonate : DiEthyl Carbonate*
EIS	*Electrochemical Impedance Spectroscopy*
f_c	*Characteristic frequency*
GCD	*Galvanostatic charge/discharge*
JCPDS	*Joint Committee on Powder Diffraction Standards*
LFP	*Lithium iron phosphate ($LiFePO_4$)*
LTO	*Lithium titanate Oxide ($Li_4Ti_5O_{12}$)*
NHE	*Normal Hydrogen Electrode*
NMC	*Nickel Manganese Cobalt Oxide*
NMP	*N-Methyl-2-pyrrolidone*
PVD	*Physical Vapour Deposition*
PVdF	*Polyvinylidene difluoride*
RC	*Resistance-capacitor*
R_{CT}	*Charge transfer resistance*
R_{EL}	*Electrolyte resistance*
SEI	*Solid electrolyte interface*
SEM	*Scanning electron microscopy*
SLG/FLG	*Single-/few-layer graphene*
SoC	*State of Charge*
SS	*Solid State*
TRL	*Technology Readiness Level*
WJM	*Wet-jet milling*
XRD	*X-ray powder diffraction*
Z_{DC}	*Impedance in DC mode*
Z_{mesh}	*Impedance contribution of the mesh and electrolyte in the pores*
τ	*Characteristic time constant*

1. Introduction

WP2 relates to a sensing technology consisting of printed reference electrodes, enabling *in situ* EIS (Electrochemical Impedance Spectroscopy) and reliable *in operando* measurements of the electrolyte conductivity and its change during the cell operation.

The main objective of Task 2.4 is to characterise the printed electrodes with different geometries, as prepared in Task 2.2 and fully described in deliverable D2.2. The morphological and structural properties of the produced electrodes were characterised by BDM with several techniques, while performing a full set of electrochemical characterizations (cyclic voltammetry-CV, Galvanostatic charge/discharge-GCD- cycling and EIS). A sensor working as reference electrode must possess stable voltage in the cell working conditions. For this reason, two different chemistries were chosen (Lithium Iron Phosphate -LFP- and Lithium Titanate Oxide -LTO-) for the printed sensors[1].

Both LFP and LTO are presenting a two-phase lithium intercalation/deintercalation reactions during charge and discharge processes, which result as a potential plateau and, thus, a stable equilibrium potential. Several cells were assembled by POL to select the best performing sensing reference electrode in term of materials (LFP and LTO), formulations (LFP/LTO with different Polyvinylidene difluoride -PVdF- and single-/few-layer graphene -SLG/FLG- contents) and cell configuration (Nickel Manganese Cobalt Oxide -NMC-/sensor/Li or graphite).

The results achieved were fundamental to get information on the as-produced sensing reference electrode, as well as on their stability and possible degradation during operation at different temperatures and cycling procedures. The impedance contribution of the printed reference electrodes was properly modelled through a mesh-like electrical equivalent circuit. Different generation of sensors were designed and evaluated, optimizing a reference electrode based on LTO. The pre-conditioning treatment of the optimized LTO-based reference electrode was screened to attain a reliable control of its equilibrium potential in full cells. The NMC/graphite cells were assembled with the designed printed reference electrodes, showing the possibility to monitor the potential of the battery electrodes, while performing in situ operando electrochemical characterization of the cell components, in line with the proposals of Battery2030+ initiative.

2. Physicochemical characterization

The selection and characterization of the materials used for the formulation of the printed reference electrodes has been reported in deliverable D2.1. The present document focuses on the characterization of the full printed reference electrodes, whose formulation has been described in deliverable D2.2, in which preliminary electrochemical characterization of the reference electrode was also reported and discussed.

The structural properties of printed reference electrodes are assessed by means of XRD (X-Ray Diffraction). Figure 1 reports the XRD patterns measured for representative SLG/FLG-based reference electrodes using LTO and LFP as active materials with a well-defined two-phase lithiation behaviour. The full formulation of the reference electrodes can be found in deliverable D2.2. Figure 1a shows that the diffraction peaks of an LTO-A reference electrode. The peaks match those of cubic spinel phase LTO (JCPDS Card No. 26-1198). In particular, the diffraction peaks at 2Θ around 18.4˚, 30.1˚, 35.6˚, 37.0˚, 43.4˚, 47.3˚, 53.9˚, 57.3˚, 63.1˚, 66.0˚, 74.2˚, 75.1˚, 79.3˚, and 82.3˚ are assigned to the (111), (220), (311), (222), (400), (331), (422), (333), (440), (531), (533), (622), (444) and (551) planes of spinel LTO, respectively.[2,3] In the XRD pattern, the additional peaks between 20° and 30° are attributed to the SLG/FLG and carbon black (CB) in the structure of the LTO-A electrode[4,5] Figure 1b reports the XRD pattern measured for the LFP-A reference electrode. The sharp peaks located at 17.1°, 20.8°, 22.9°, 24.2°, 25.5°, 29.9°, 32.2°, 35.8°, 36.6°, 38.0°, 39.7°, 39.9°, 42.3°, 48.9°, 50.2°, 50.3°, 53.2°, 55.3°, 55.5°, 58.2° and 61.6˚ correspond to the (200), (101), (210), (011), (111), (211), (301), (311), (121), (410), (221), (401), (112), (022), (212), (131), (222), (412), (610), (331) and (430) reflections of LFP nanoparticles, respectively, matching the XRD pattern of cubic LFP (JCPDS Card No. 40-1499).[6] As for the case of LTO-A, the additional peaks located between 20° to 30˚ corresponds to the reflection of the CB and SLG/FLG flakes, even though these peaks can overlap with those of LFP nanoparticles.
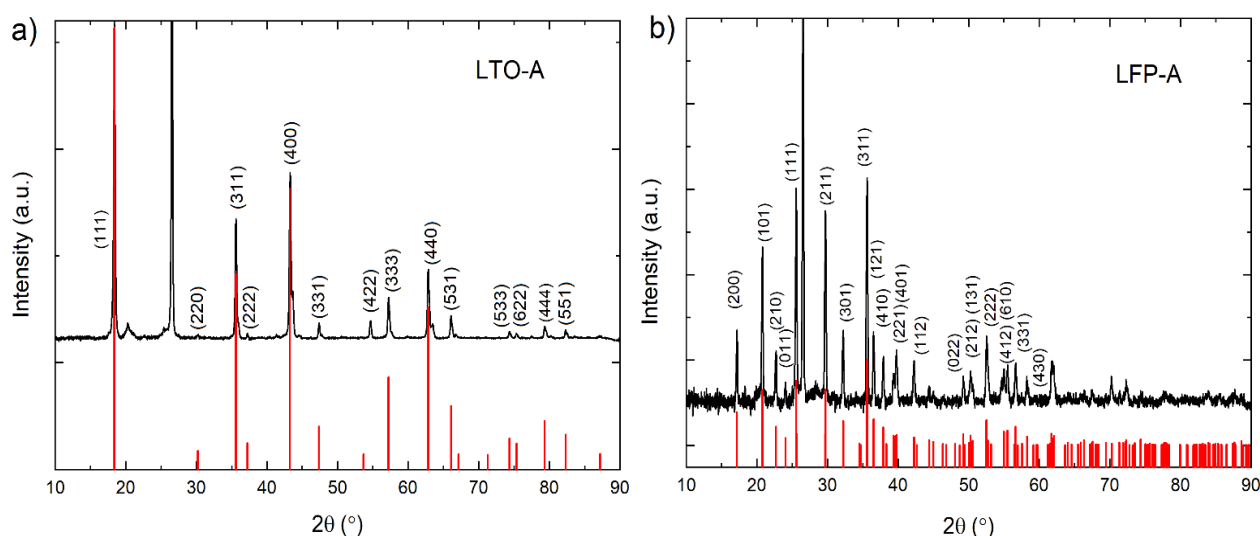
Figure 1. XRD patterns measured for a) LTO-A and b) LFP-A reference electrodes. The reference pattern of cubic spinel phase LTO (JCPDS Card No. 26-1198) and cubic LFP (JCPDS Card No. 40-1499) are also reported in red.

Raman analysis was used to inspect the structural characteristics of the printed reference electrodes. Figure 2 compares the Raman spectra measured for LTO-A and LFP-A reference electrodes, together with those of each material composing the electrode formulation (i.e., LFP, LTO, PVdF, SLG/FLG and CB). In CB and SLG/FLG spectra, the peak at 1350 cm^{-1} corresponds to the carbon D-band, representing the disorder carbon and the breathing modes of the sp^2 hybridized carbon rings.[7,8] The peak at 1585 cm^{-1} is attributed to the G band, corresponding to the E$_{2g}$ phonon at the Brillouin zone centre.[4,9] The 2D peak located around 2700 cm^{-1} is the second order of

the D peak, and it appears also in the absence of D peak,[9,10] since no defects are required for the activation of two phonons with the same momentum, one backscattered from the other.[11] By the analysis of the 2D peak, the thickness of the graphene flakes can be estimated.[9,11].
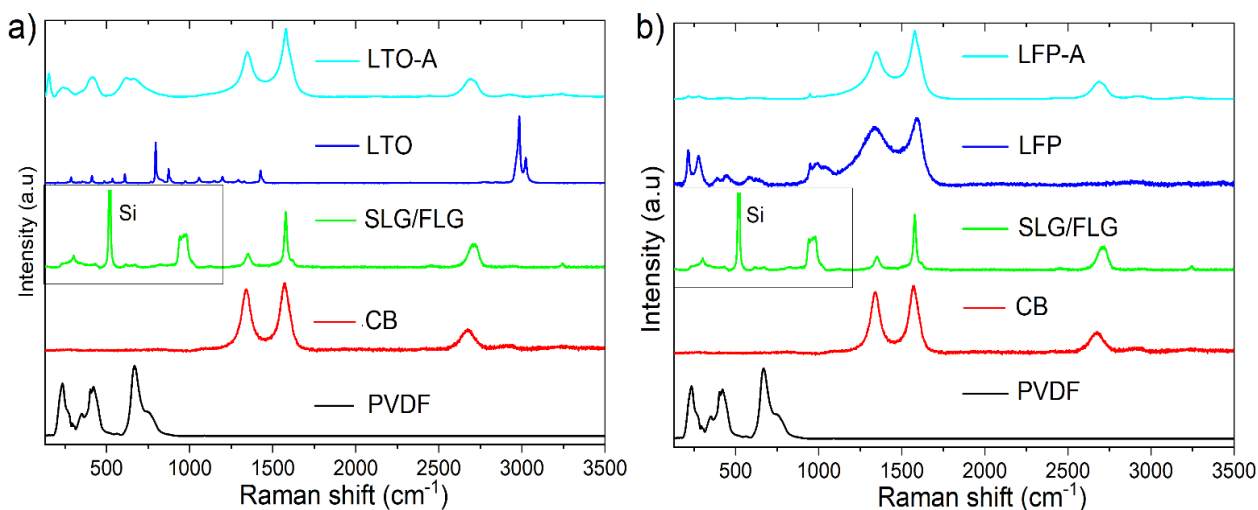
Figure 2. Comparison between the Raman spectra of a) LTO-A and b) LFP-A reference electrodes. The spectrum of each material composing the reference electrodes (i.e., SLG/FLG, CB, PVD, LTO and LFP) are also reported.

More in detail, 2D peak is made of two contributions, named $2D_1$ and $2D_2$.[10] The intensity of the $2D_2$ is around twice that of $2D_1$[11] in graphite and multi-layer graphene (> 5 layers). Few-layer graphene, instead, has a $2D_1$ peak which is intense than the $2D_2$.[11] Lastly, SLG exhibits a 2D peak given by a single sharp contribution attributed to $2D_1$.[11] Thus the Raman spectrum of SLG/FLG confirms that the sample is mainly composed by FLG flakes, in agreement with the material characterization already reported in deliverable D2.1. The Raman spectra of PVdF powder shows the characteristic peaks at 246, 416 and 648 cm^{-1}.[12] In the Raman spectrum of the LTO (Figure 2a), the three peaks at 222, 278, and 352 cm^{-1} correspond to the F_{2g} modes, the peaks at 617 and 755 cm^{-1} correspond to the A_{1g} modes, and the peak at 419 cm^{-1} correspond to the E_g mode.[3,13] The Raman spectrum of the LTO-A reference electrode mainly shows the peaks associated SLG/FLG, CB and PVdF, masking those of LTO. In Figure 2b, the Raman peaks at 215, 281, 390, 446, 586 and 642 cm^{-1} are the fingerprint of the orthorhombic symmetry of LFP.[14] In addition, the peaks located at 992, 1,052, and 948 cm^{-1} correspond to the anti-symmetric ($v3$) and symmetric ($v1$) stretching of the P–O bonds.[15]. Also in this case, the peak of carbonaceous materials masks the peaks of LFP in the LFP-A reference electrode.
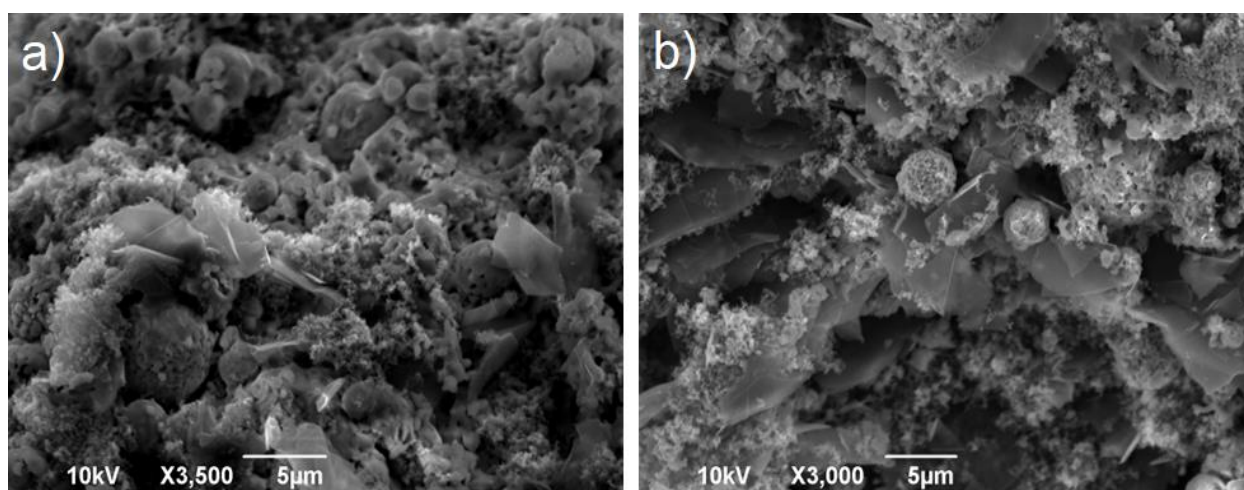
Figure 3. SEM images of the a) LTO-A and b) LFP-A reference electrodes.

The morphology of the printed reference electrode was evaluated through SEM measurements. Figure 3 shows the cross-sectional SEM images of the LFP-A and LTO-A reference electrodes, indicating a homogeneous dispersion of the LFP/LTO nanoparticles and SLG/FLG flakes within the electrode structure, without showing any relevant material aggregation. These data are consistent with the active material utilization verified through electrochemical characterizations (i.e., GCD analyses) reported in deliverable D2.2. In the electrode structure, the LFP/LTO nanoparticles are wrapped by SLG/FLG flakes and CB, creating an electrically conductive network with low electrical resistivity (< 0.1 $\Omega \times$cm). In particular, the interconnection of SLG/FLG and CB promotes the electron transport during electrochemical reactions, thereby enhancing the electrochemical performance of the printed reference electrodes and permitting their modelling through mesh-like equivalent electrical circuit, as discussed in deliverable D.2.2 and described in section 3.

3. Reference electrodes modelling

The theoretical modelling of the impedance of the reference electrodes must be considered to provide reliable estimation of half-impedance of the batteries. Such reference electrode modelling intrinsically enables the optimal geometry/configuration of the reference electrode to be designed without jeopardizing electrochemical experiments and analysis. In fact, proper location, shape, and morphology of a reference electrode must minimize or fully avoid common measurement artifacts, e.g., inductive loops and other impedance spectra distortions.

Various geometries and locations of conventional bulky reference electrodes (*e.g.*, point-like, wire, ring-shaped, coaxial and mesh reference electrodes) have been evaluated for the Li-ion batteries in previous literature[16,17] aiming at assessing the origin of EIS measurement artifacts. The presence of non-uniform current densities ascribed to geometric and electrochemical asymmetries can result in the sampling of various equipotential surfaces between the counter electrode and work electrode, leading to artifacts. In an ideal case, there would be no geometric asymmetry between the counter and working electrodes.[16] Instead, point-like and ring-shaped reference electrodes are subject to the geometric asymmetries (*e.g.*, radially inhomogeneous current distributions). For coaxial reference electrodes,[16] artifacts in EIS spectra are dependent from the thickness of separators and are associated to electrode misalignments and electrolyte wetting of the lateral surface of the electrodes. The geometric asymmetry effects are considerably decreased in wire and mesh-like reference electrodes. However, in the stacked cells, the ring-like reference electrode could deform the positive and negative electrodes causing an uneven distance between adjacent electrodes and geometric asymmetries, leading to measurement artifacts. Moreover, the bulky nature of this electrode can block the ion transport, causing Li^+ concentration gradients, which are cause of localized overcharging (overpolarization) of the electrodes[16–18].

By considering their porous structure, as well as their low electrical resistivity (< 0.1 $\Omega \times cm$), the printed reference electrodes, placed between two Celgard 2500 separators, were modelled as an ultrathin (non-bulky) mesh-like electrode. In this model, the ions can either travel in the electrolyte through the openings of the mesh or being subject to oxidation and reduction reactions at the two sides of the mesh. The ideal mesh case must have a thin and large opening ratio to decrease Li-ion blocking effects[17]. Such effects are intrinsically mitigated in the designed printed reference electrodes. In fact, their porous structure can avoid macroscopic (over 100 µm-scale) ion blocking effects. Thus, according to [11], assuming that electronic conductivity is higher than electrolyte conductivity (~0.01-0.1 S cm^{-1}) that is verified for the produced reference electrode having a conductivity between 10-100 S cm^{-1}, the impedance contribution of the mesh-like electrode and electrolyte in the pores (Z) is calculated as:

$$Z = \frac{1}{1 + i\omega\tau \, R_{EL}/(R_{CT} + R_{EL})} \times \frac{R_{CT}.R_{EL}}{R_{CT} + R_{EL}}$$

R_{CT} is the charge transfer resistance of the electrode, and R_{EL} is the resistance electrolyte inside the electrode pore (*e.g.*, mesh openings), and τ is the electrode characteristic time constant (given by the product between R_{CT} and the electrode capacitance -C-). Noteworthy, the as-modelled electrode impedance is still the one of resistance-capacitor (RC) circuit with a characteristic frequency (f_C) given by:

$$fc = \frac{2\pi}{\tau}$$

To reach higher f_C (*e.g.*, > 10 kHz needed for common EIS analysis of batteries' electrodes), R_{EL} must be minimized, and this can be done by reducing the reference electrode thickness.

In addition, the impedance in DC mode (Z_{DC}), given by:

$$Z_{DC} = \frac{R_{CT} \cdot R_{EL}}{R_{CT} + R_{EL}}$$

must be also minimized to reduce ohmic losses at high C-rate cycling operation.

The R_{EL} was extrapolated by measuring the high-frequency resistance of symmetric cells with SS electrodes (Figure 4) through EIS measurements.
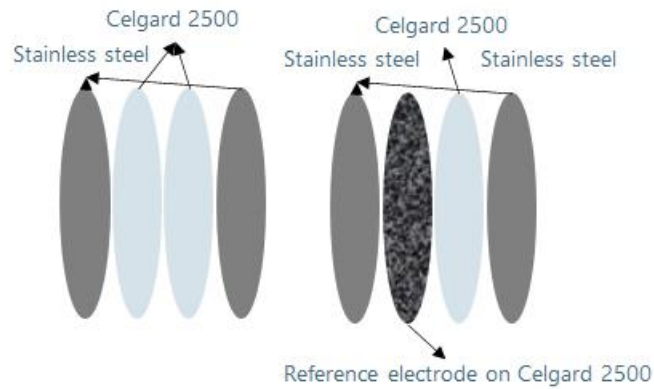
Figure 4. Sketch of the symmetric cells with SS electrodes used for the evaluation of R_{EL}.

The R_{CT} and τ could be calculated from EIS analysis of symmetric cells (Figure 5) using 2 printed reference electrodes (for example, deposited on Cu or Al foil substrates to simplify the cell assembly).

Figure 5. Sketch of symmetric cells with printed reference electrodes (on Al or Cu substrates) used for the evaluation of R_{CT} and τ.

4. Electrochemical testing

4.1   Samples definition

As described in deliverable D2.2, BDM formulated several printed reference electrodes, resulting in different electrical characteristics. In particular, resistivities between 0.06 and 1.6 Ω×cm were obtained by incorporating SLG/FLG flakes as highly conductive additives, showing beneficial advantages in terms of electrical conductivity of the r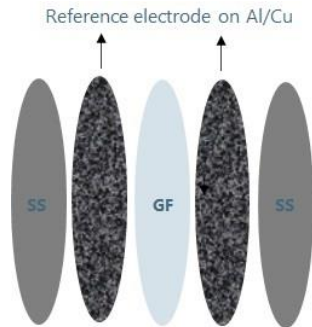eference electrode compared to prototypical CB (*e.g.*, SuperP). The most conductive electrodes were then selected to continue the Task 2.4 (and Task 2.3) activities and were sent to POL for their further electrochemical characterization. The formulation of the printed reference electrodes, reported in this deliverable, is recalled in Table 1:

Table 1. Sample composition and names.

Product name	Component content (wt%)				Resistivity (Ω·cm)
	Active material (LFP/LTO)	PVdF	FLG/SLG	CB	
LFP-A	25	25	25	25	0.060
LFP-A*	25	25	25	25	
LFP-B	50	25	12.5	12.5	0.065
LFP-D	65	10	12.5	12.5	0.088
LTO-A	25	25	25	25	0.066
LTO -B	50	25	12.5	12.5	0.109
LTO -D	65	10	12.5	12.5	0.402

Note: LFP-A* is a modification of LFP-A, in which SLG/FLG flakes produced through 5-pass WJM protocol have been replaced with SLG/FLG flakes produced through a 1-pass WJM protocol (see details in deliverable D2.1).

4.2   Experimental test protocols

The following list reports the electrochemical tests/analyses that have been performed to study the electrochemical behaviour of the printed reference electrodes when incorporated into Li-ion battery cells:

- Evaluation of the impedance parameters of the reference electrode through EIS measurements, as described in section 3.
- Evaluation of cyclability of cells in coin and pouch formats using different separator configurations: i) 2 pristine Celgard®2500 (uncoated separators) and ii) reference electrode coated Celgard®2500 plus pristine Celgard®2500, simulating real embedding conditions of the sensing electrodes.
- "Plating and stripping" experiments to assess the effect of the presence of printed reference electrode on lithium-ion transport dynamics in standard coin cells, using Li/LFP-coated Celgard®2500 + Celgard®2500 /Li symmetric cell configurations.
- Reference electrode preconditioning through GCD protocols to unravel the equilibrium potential stabilization.
- Evaluation of the stability of reference electrode potential over time and monitoring of anode and cathode potentials vs. reference electrodes using a three-electrodes cell assembly with either LFP and LTO-based printed reference electrodes.

All voltage values are reported vs Li/Li+ (-3.05V vs NHE – Normal Hydrogen Electrode).

4.3   Evaluation of the reference electrode impedance parameters

The calculated EIS impedance parameters of the printed reference electrodes are reported in Table 2. Based on the electrical modelling described in section 3, the obtained results confirm that the f_c of the reference electrodes are higher than 400 kHz. These values are adequate to carry out valuable EIS measurements of battery electrodes. Moreover, Z_{DC} values indicates that the electrode adds marginal series resistance contribution to the battery, even less than 1 Ω cm^2 in some case. Importantly, in a full cell, the series resistance contribution of the printed reference electrodes can be minimized by decreasing their geometric area and thickness. Overall, these results suggested that the reference electrodes feature adequate electrochemical characteristics to perform in-situ/in-operando electrode EIS and potential monitoring measurements.

Table 2. EIS impedance parameter values of reference electrodes.

Reference electrode	Thickness (µm)	R_{EL} ($\Omega.cm^2$)	R_{CT} ($\Omega.cm^2$)	C ($\mu F/cm^2$)	τ (1/s)	f_c (kHz)	Z_{DC} ($\Omega.cm^2$)
LFP-A	50	1.5	6.90	2.0	2.45×10^{-6}	2563	1.23
LFP-B	50	7.5	12.95	1.8	8.54×10^{-6}	735	4.74
LFP-D	50	0.6	19.82	1.35	7.85×10^{-7}	8000	0.58
LTO-A	50	1.6	2.11	17.29	1.55×10^{-5}	405	0.90
LTO-B	50	0.3	2.54	18.09	4.84×10^{-6}	1297	0.26
LTO-D	50	9.1	1.79	8.01	1.19×10^{-5}	527	1.49

4.4   Two-electrodes cell configuration assembly and characterization

Two-electrodes cells were assembled with two different scopes:

-   To optimize the cell assembly, both in pouch and coin cell format, with the electrode materials used in the project and supplied by VAR
-   To fully characterize the printed reference electrodes produced by BDM, based on LFP and LTO, before using them as sensors in the three-electrodes cells

4.4.1   NMC-622/Graphite pouch and coin cells assembly optimization

Full pouch cell assembly and optimization

To assemble the full cells, the electrode active materials, including NMC-622 cathode and graphite anode, were supplied by VAR. A graphite anode of 2.4×2.4 cm and an NMC-622 cathode of 2.0×2.0 cm were cut by punching them from larger samples. The different size of the electrodes ensured the full covering of the cathode by the anode. LiPF$_6$ 1M EC:DEC 1:1 was used as electrolyte. During cycling, the cells were clamped with a stable pressure to ensure a proper contact between the electrodes and other cell components. The applied pressure was optimized to be high enough to ensure a proper wetting of electrodes, and to avoid possible damage of the separator. Figure 6 reports a scheme of a full pouch cell and a picture of the pouch cell components, before being sealed into the whole pouch cell format.
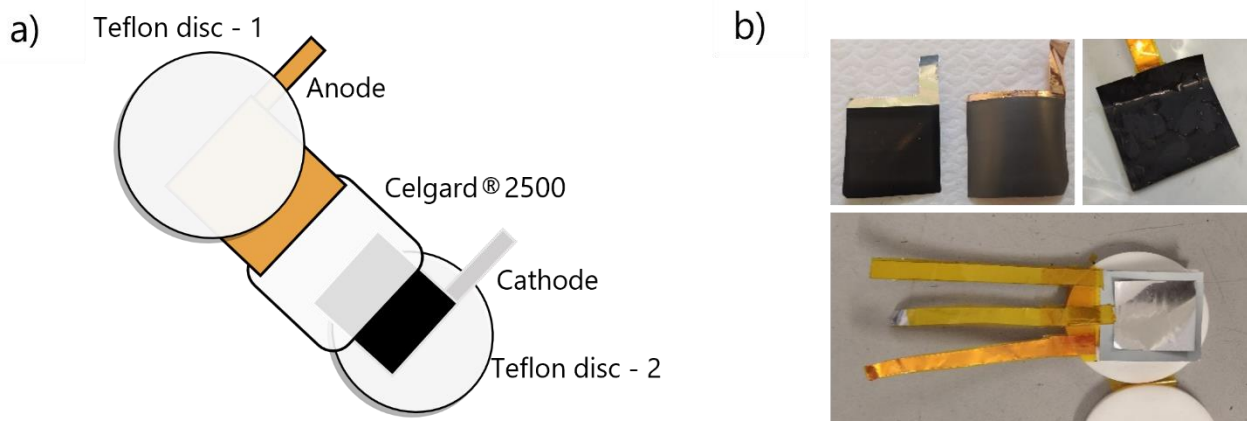
Figure 6. a) Schematic of the pouch cell assembly; b) pictures of graphite anode and NMC-622 cathode, rinsed graphite anode and cell assembly immediately before to be sealed in Ar atmosphere.

Full coin cell

For the sake of comparison, coin cells were assembled according to the configurations reported in Figure 7. Coin cells serve as control samples for pouch cells, because the formers are easier to assemble and therefore more reproducible than pouch cells. Electrodes diameters were 15 mm. Proper amount of electrolyte (50 µL) was added and a sealing pressure of 5000 N was applied with an MTI semi-automatic crimper.
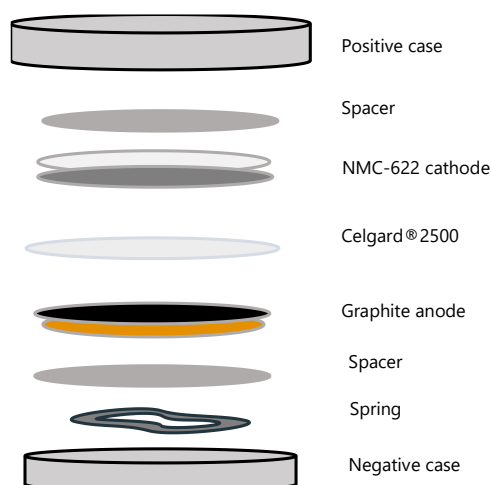

Figure 7. Schematic of a coin cell (control sample).

Cell tests and pouch/coin cells comparison

Galvanostatic charge/discharge cycling tests were performed using galvanostat/potentiostat. The test protocol consisted of 5 GCD cycles at C/10 C-rate and 5 GCD cycles at C-rate of C/5. The values of the applied currents were calculated by considering the theoretical capacity of the electrodes, as provided by VAR. Table 3 reports the charge and discharge capacities of both coin and pouch cell configurations, as extrapolated from GCD cycling. The data clearly indicate that the charge/discharge profiles were reproducible during the whole GCD

cycling at both C/10 and C/5 rate. In addition, the capacity retention of the pouch cell over cycling is slightly better than the one of the coin cells, validating our hand-made pouch cell assembly for the Task 2.4 activities.

Table 3. Charge and discharge capacities of the coin and pouch cells with NMC-622 cathodes and graphite anodes.

C-rate	Cycle Number	Coin cell		Pouch cell		ΔC_{Charge} (%)	$\Delta C_{Discharge}$ (%)
		Charge Capacity (mAhcm^{-2})	Discharge Capacity (mAhcm^{-2})	Charge Capacity (mAhcm^{-2})	Discharge Capacity (mAhcm^{-2})		
C/10	1	3,47	2,86	3,49	2,95	1,9	8,8
	2	2,87	2,81	3,03	2,97	15,8	15,4
	3	2,90	2,86	3,00	2,94	10,1	8,6
	4	2,88	2,84	2,98	2,93	9,3	9,1
	5	2,85	2,81	2,94	2,90	9,2	9,4
C/5	6	2,76	2,71	2,84	2,75	8,5	4,1
	7	2,72	2,70	2,78	2,71	6,4	1,8
	8	2,70	2,70	2,75	2,77	4,9	7,4
	9	2,71	2,69	2,78	2,75	5,4	5,7
	10	2,70	2,68	2,74	2,77	8,3	8,6

Figure 8 reports the comparison between the GCD profiles measured for pouch and coin cells at C/10 and C/5.

The curves are showing a similar behaviour at low C rate and some differences in the capacity at C/5. Coin cells can be better sealed in comparison to pouch cells at lab scale and the pressure on the electrodes is well reproducible.
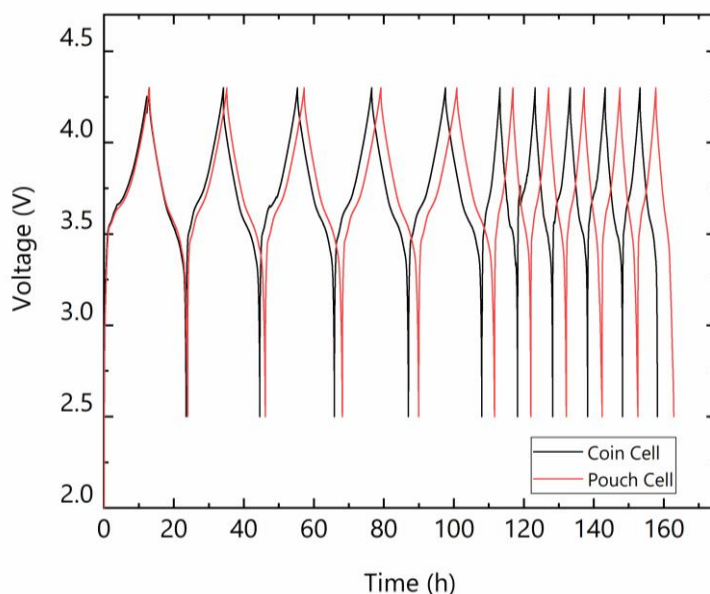

Figure 8. Comparison of the GCD profiles for pouch and coin cell at C/10 and C/5 (5 cycles for every C-rate).

4.4.2   Electrochemical characterization of LFP-coated Celgard®2500 sensor

Different LFP-based reference electrodes were produced, as shown in Table 1. All these samples were fully characterized and, in this deliverable, only the most meaningful measurements are reported.

The scope of this test is to assess the kinetics of lithium dissolution (stripping) and deposition (plating) of/at the lithium metal anode, evaluating the effect of the presence of printed reference electrodes on the reactions' overpotentials.18 In fact, in lithium plating and stripping processes, the lithium ions transport between the electrodes (across the separator) and in the electrode/electrolyte interphase, such as the SEI, together with the kinetic hindrance of the lithium-ion reduction and oxidation processes at the electrode itself, determine the charge transfer resistance, and, thus, the measured reaction overpotentials.

In symmetric cells using Li foils as both anode and cathode, lithium plating/stripping directly monitors Li+ transport through the separator system, which can also include the printed reference electrode. Figure 9 compares the voltage profiles of the symmetrical cells with two Celgard®2500 and one Celgard®2500 plus LFP-A Celgard®2500 at current densities of 0.1, 0.5 and 1 mA cm-2. Both charge and discharge times were set at 1 h.

Because the results achieved in the two-cell configurations are very similar, the addition of the reference electrode does not introduce significant ohmic resistance to the whole cells, in agreement with electrical modelling reported in section 3, as well as the reference electrode impedance parameters shown in Table 2, reported in section 4.3.
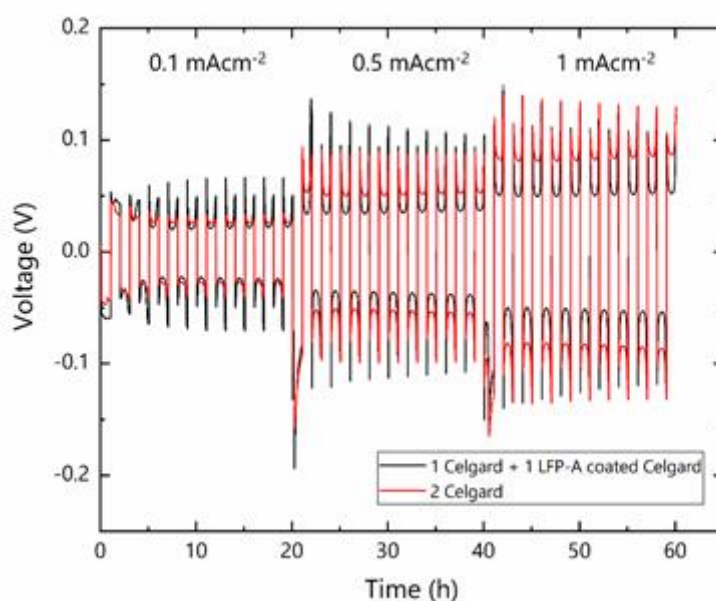

Figure 9. Lithium plating/stripping measurements at different current densities of LFP-coated Celgard®2500 plus an additional Celgard®2500 and for a cell using two identical uncoated Celgard®2500.

4.4.3 Preconditioning treatment of printed reference electrode

In order to ensure the long-term stability of the potential of the reference electrodes and according to literature data, a supplementary electrochemical treatment (preconditioning) was considered before the three-electrode cell configuration tests. In fact, the printed electrode has shown an initial voltage around 3.2 V, which is lower than the expected value of 3.5 V and it is not fully stable.

Experimentally, the reference electrodes were preconditioned exploiting a Constant Current-Constant Voltage (CC-CV) protocol, as shown in Figure 10:

- charging at a constant current (C/10) until its voltage reaches 3.5 V (50% of SoC, based on the nominal capacity of the printed reference electrode),
- charging at a constant voltage for 5 h.
- resting for 10 h and measurement of the voltage evolution until stabilization.
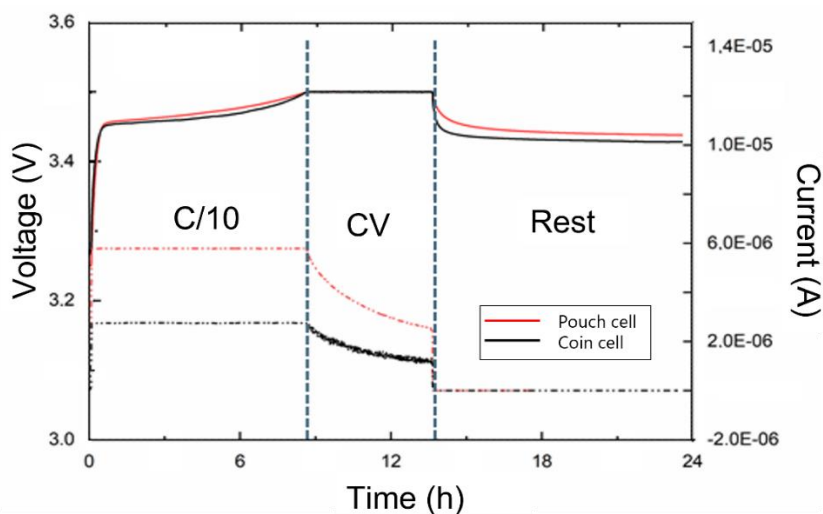

Figure 10. Voltage (vs. Li/Li⁺) and current profiles of the LFP-A in pouch and coin cell configurations during the preconditioning procedure.

The advantages of the preconditioning of the reference electrodes were assessed by monitoring Li anode potential in NMC-622/Li battery. The characterization protocols reported in section 4.5.2 for the same analysis was slightly modified to add a rest of 3 h at every C-rate change (C/10, C/5, C/2, 1C). Figure 11 reports the voltage profiles recorded at C/10, indicating that the LFP potential vs Li/Li⁺ reached the initial value (approximately 3.41 V), enabling the accurate monitoring of the potential of battery electrodes thanks to its stable equilibrium potential around its 50% SoC.
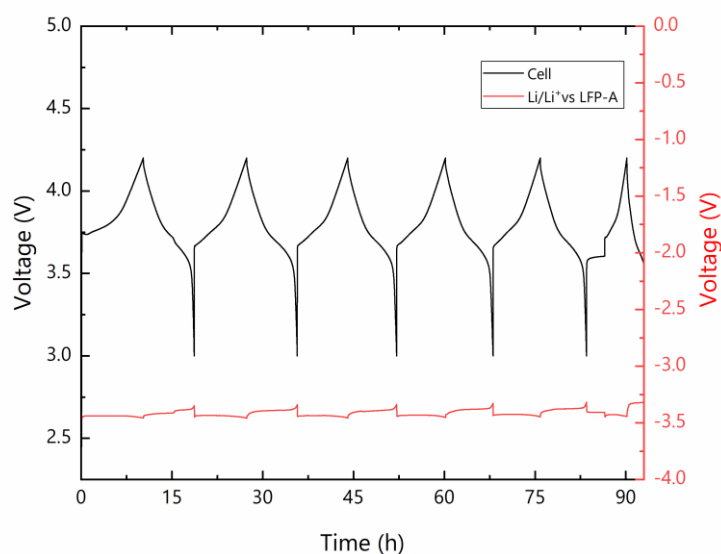

Figure 11. Cell voltage profile (black line) and LFP-A potential Vs. Li/Li+ during cell cycling at C/10 rate.

4.4.4 Electrochemical characterization of LTO-coated Celgard®2500 sensor and its optimization as reference electrode

Also, in the case of LTO a preconditioning step is necessary as formation step and to stabilize the equilibrium potential of the printed reference electrode. As reported in literature,[20] a pre-lithiation step with using metallic lithium anode, to reach 50% of its capacity, is needed to stabilize the materials in a potential region in which the voltage curve is very flat.

The pre-conditioning step of the reference electrode has been performed using the following protocol: (i) charge at maximum voltage at C/10, with the current evaluated according to the value of capacity of the 4th cycle of the previous step, (ii) discharge at 50% of State of Charge (SoC) at C/10 and (iii) final rest of 10 hours.

Figure12a-b shows the results of pre-conditioning step. Both LTO-A and LTO-B are stable after pre-lithiation and their potential values during cycling is flat around 1.55 V: this value is at a good distance from the reduction potential of NMC and the one of graphite or Lithium, making LTO a very good candidate as reference electrode for Li-ion cells in general.
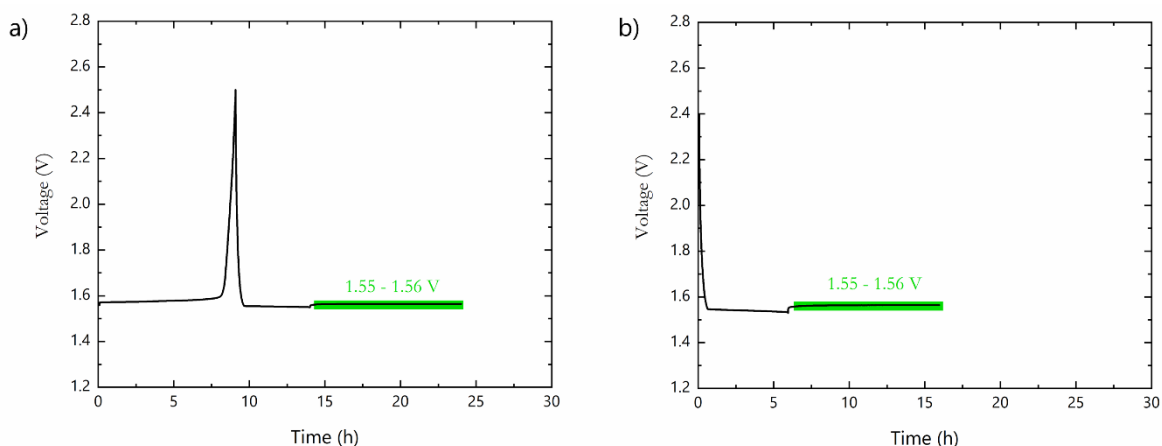

Figure 12. Pre-conditioning of a) LTO-A and b) LTO-B.

Pouch cells with metallic lithium as anode and NMC622 as cathode with LTO sensors as reference electrode were assembled and the galvanostatic cycling tests are reported in Figures 13 and 14. The data evidence the good performance of LTO-B reference electrode, which shows a high stability under cycling. Therefore, LTO-B was selected as the sensor to build the full cell in pouch cell configuration.
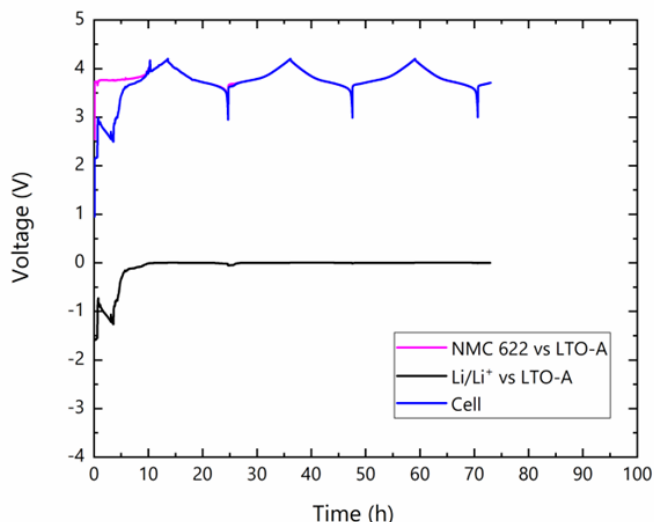
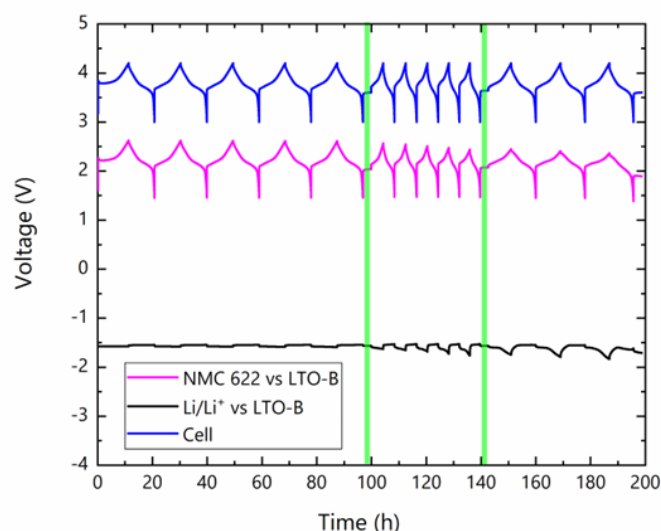**Figure 13. Galvanostatic cycling of LTO-A.**

Figure 14. Galvanostatic cycling of LTO-B.

One pouch cell using Celgard®2500 as separator and without sensors and another pouch cell with the LTO-B sensor were assembled to evaluate the influence of LTO-B sensor on the full cell cycling. The two different cells have not shown differences of the capacities during cycling, see Figure 15. It was concluded that: LTO-B reference electrode (thickness ~200 µm) did not contribute to the increase of the overall cell capacity and did not affect the performance of the pouch cell cycling.
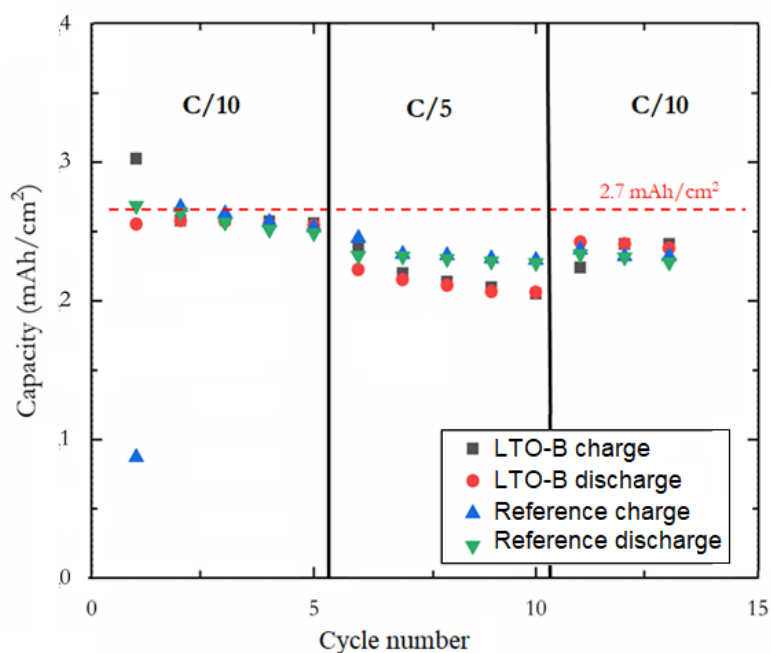

Figure 15. Capacity comparison between 2Celgard®2500 and LTO-B pouch.

In order to better evaluate the blocking effect of LTO sensors[17] in pouch cell configuration, EIS measurements have been performed and are reported in Figure 16 which compares the behaviour of LTO-A and LTO-B sensors on Celgard separator with a dummy cell containing only 2 separators. As expected, both the cells with LTO are showing a shift of the spectra to higher real impedance values compared with the dummy cell with 2 separators. LTO-B, compared to LTO-A, shows a lower ionic resistance, so demonstrating that Li⁺ ions can flow easily

through the separator even in the presence of the printed sensor. This confirms that the pouch cell assembled with LTO-B sensor shows better performance.
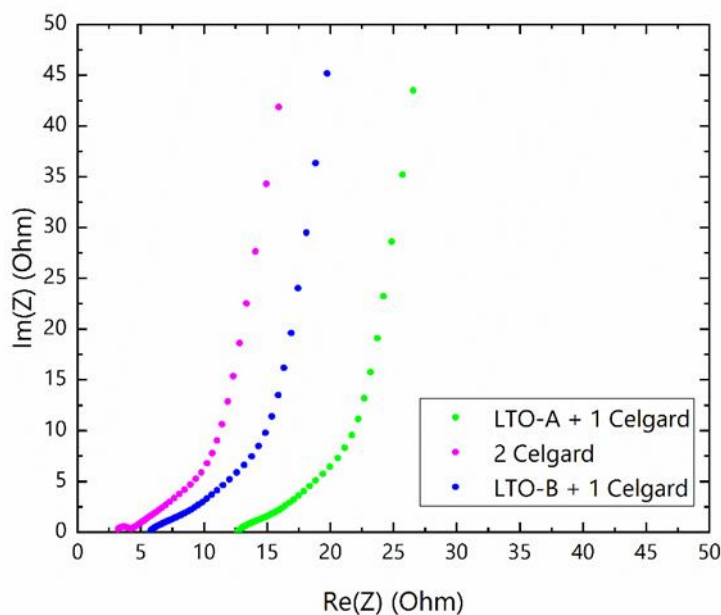

Figure 16. Impedance spectra in a Nyquist plot at 0% SoC after 12 hours of rest.

4.5 Three-electrodes cell configuration assembly and characterization

After the characterization of the sensors printed on Celgard separator, three-electrodes cells were assembled using the sensors as reference electrode to monitor the voltage of the cathode and the anode during the cell operation. After monitoring the voltage of NMC cathode and the one of graphite anode in full cell, a preliminary step to stabilize the voltage of the reference electrode was studied to find the optimized conditions. Finally, the full cell with the best performing sensor was assembled, see Figure 17, and characterized.
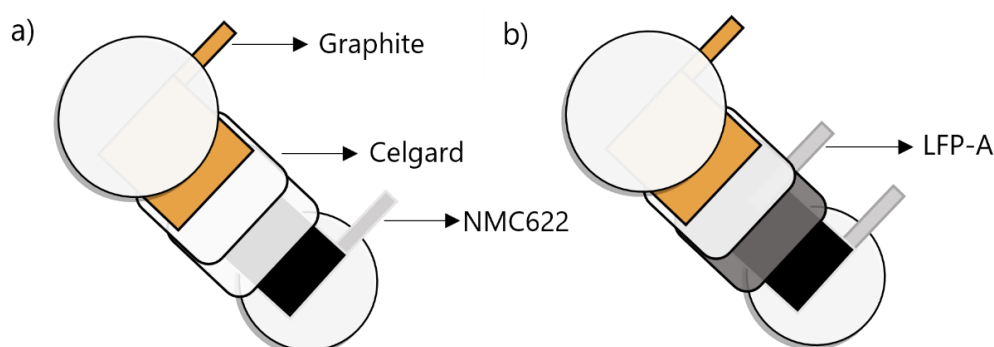

Figure 17. Sketches for three-electrode cell configuration using (a) two uncoated Celgard®2500, (b) and LFP-coated Celgard®2500 (grey) plus an additional uncoated Celgard®2500 as separators.

4.5.1 Li anode monitoring in NMC-622/Li battery

Electrode potential monitoring

A pouch cell with NMC-622 as cathode and lithium metal as anode was assembled using the separator configurations including the printed reference electrode (namely LFP-A). In this configuration, LFP-A was used

to monitor the anode potential during cell cycling. Figure 18a shows a scheme of the cell connections, while Figure 18b shows the recorded voltage profiles.
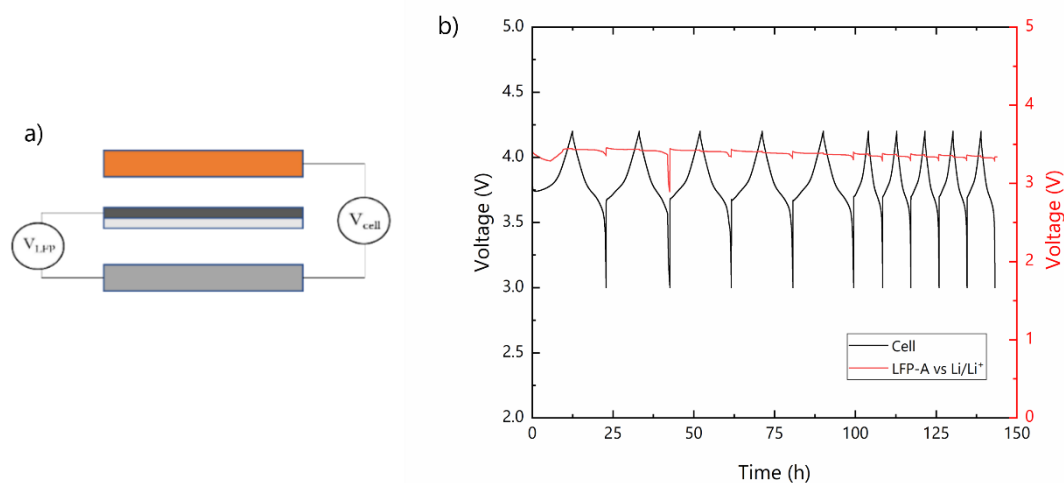

Figure 18. a) Scheme of the cell connections (Orange: cathode; Grey: anode, Dark grey: reference electrode-coated separator; Light grey: uncoated separator). b) Voltage profiles for the whole cell (black line) and the potential of the LFP-A vs. lithium metal anode (red line). The drop in LFP vs Lithium potential ad the end of the second cycle discharge is due a setup error (clamps small short-circuit because accidental contact).

A progressive decrease of LFP-A was observed during cycling. Post-mortem analysis (Figure 19) evidenced the lithium metal surface degradation in the area overlapped by the cathode due to lithium dendrites formation and electrolyte degradation. Overall, these preliminary measurements evidenced the potential of the reference electrode to monitor anode potentials, associating its profile to modification/degradation effects. It should be noticed that the printed reference electrodes were not preconditioned and used as-produced (thus, in a fully lithiated phase). Therefore, some potential changes of the printed reference electrodes caused by SEI formation and other electrochemical effects cannot be excluded at this stage. The control of the potential stability of the reference electrode through preconditioning treatment will be discussed in section 4.6.
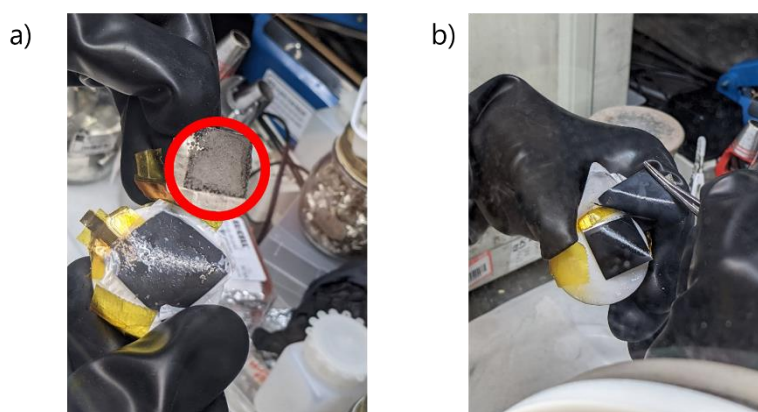

Figure 19. Post-mortem visual evaluation of NMC-622-Li cell. (a) Details of the film growth on lithium metal surface with a details of lithium corruption film in the red circle) and (b) evidence of the good conditions of other cell internal components.

4.5.2   Graphite anode monitoring in NMC-622/graphite full cell

Metallic Li anode was substituted by graphite anode in a full cell (Fig. 20a), and the graphite potential was then monitored using the LFP-A reference electrode. Except for the first cycle, the graphite potential profile is stable over cycling (Figure 20b), indicating proper cell operation. As commented in section 4.4.3, the printed reference

electrode was used as produced (thus, in a fully lithiated phase), and their potential changes caused by SEI formation and other electrochemical effects cannot be excluded. The control of the potential stability of the reference electrodes through preconditioning treatments is discussed in section 4.6.
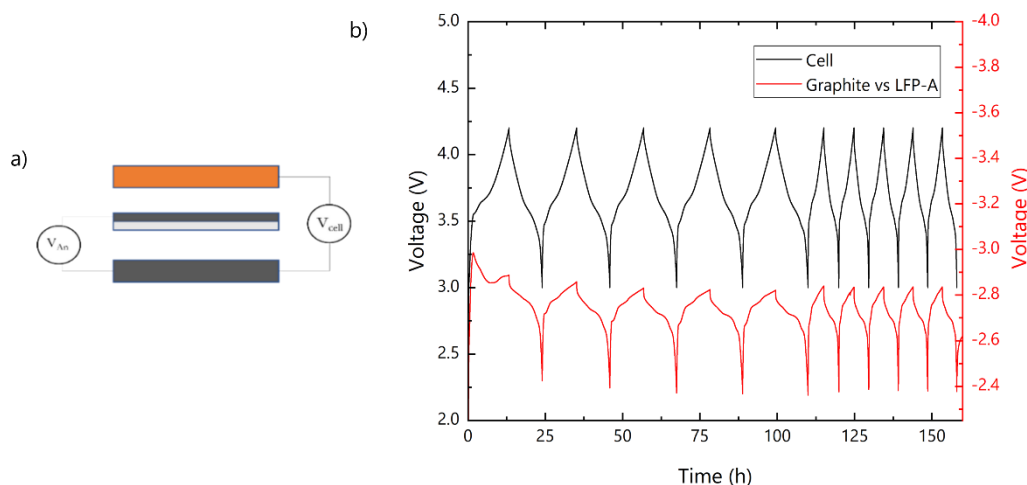

Figure 20. a) Scheme of the cell connections. (Orange: cathode; Dark grey; anode and the reference electrode-coated Celgard®2500; Light grey: uncoated separator). b) Voltage profiles for the whole cell (black line) and for the graphite anode (red line).

4.6   Optimization of LTO Sensors in full cells

After optimizing cell assemblies, including the embedding of printed reference electrode, as well as the preconditioning treatment of printed reference electrodes, and demonstrating their capability to work as reference electrodes, w further optimized the LTO sensor to demonstrate its use in different cell composition. This optimization activity was performed trying to reduce the LTO sensor thickness to increase the total energy density of the cell, tailoring the pressure applied at the latter during its cycling.

BDM produced two additional LTO-B samples with reduced thickness (54 µm) compared with the previous ones (240µm), evaluating the effect of the thickness on both the reference electrode adhesion to the Celgard®2500 and (electro)chemical properties.

Figures 21 and 22 show the results of the galvanostatic cycling performed with the two LTO-B reference electrodes, with different thicknesses (240µm and 54µm), inside half-cells with metallic lithium as the anode and NMC622 as the cathode. In particular, Figure 21 shows the galvanostatic cycling of the thicker LTO-B (named as LTO-B 240µm) and can be compared to the thinner LTO-B sample (named LTO-B 54 µm) which results of galvanostatic cycling is reported in Figure 22. The sample with lower thickness (LTO-B 54 µm - Figure 22) shows a regular voltage profile with good performances in terms of capacities and coulombic efficiency. In addition, LTO-B 54µm shows a better wettability and adhesion, and therefore, it is chosen to assembly the final pouch cell.
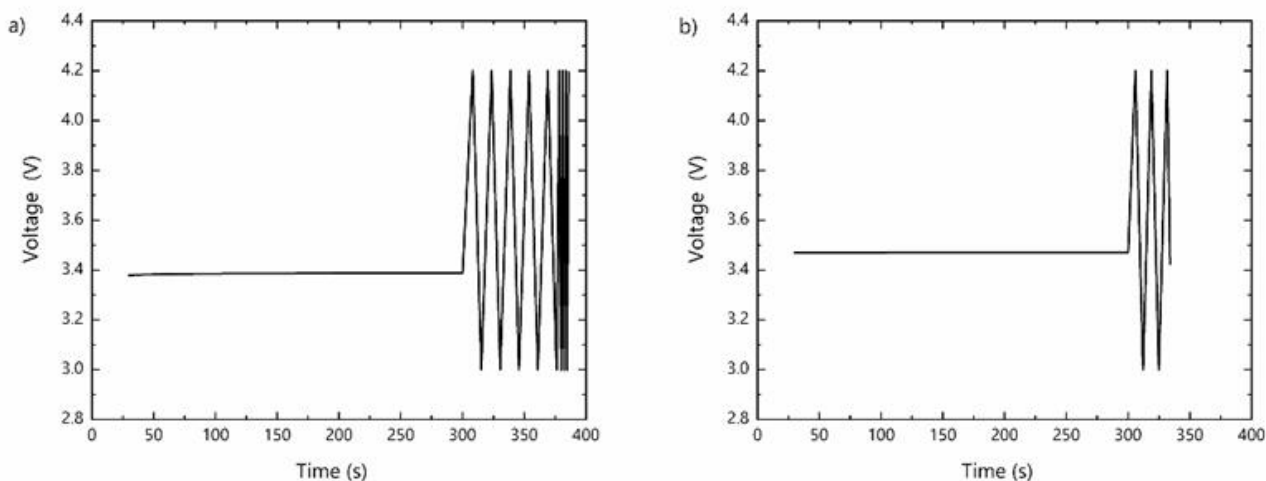
Figure 21. Galvanostatic cycling a) at C/10 and C/5 and b) at C/5 of Li - LTO-B 240µm - NMC622.
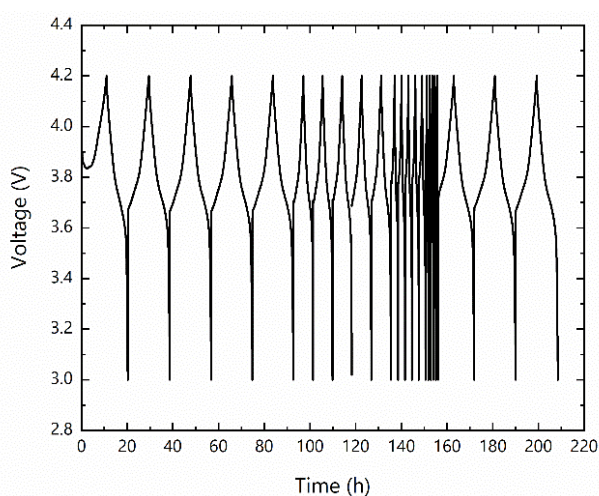

Figure 22. Galvanostatic cycling at C/10, C/5, C/2, 1C and C/10 of Li - LTO-B 54µm - NMC622.

In addition, also the effect of the amount of the active material (LTO) was studied when we compared the electrochemical characteristics of LTO-A sample with 25%wt of active materials and LTO-B with 50%wt of active material, as previously reported in Table 1.

The electrochemical performance of the full cell (NMC/LTO on Celgard®2500/Celgard®2500-Graphite) was tested in CR2032 coin cells. All the cells were cycled at constant increasing C-rates at room temperature in the range 3V-4.2V. Finally, to enable a good permeation of the electrolyte, a preliminary rest step of 12 hours was set before cycling.

Figure 23 shows the galvanostatic cycling capacity of the complete coin cells:
1) NMC622 / 2 Celgard®2500 / Graphite
2) NMC622 / LTO-A on Celgard®2500 / Celgard®2500-Graphite
3) NMC622 / LTO-B on Celgard®2500 / Celgard®2500-Graphite

The three cells have specific capacity above 2.5mAh/cm^2 at current rate of C/10 maintaining good cyclability, also at higher C rates. We have indeed stressed the cells, cycling them at higher current rates (up to 1C) to evaluate the performance of the full cells. The LTO-B sensors is loosing capacity at 1C, compared to the other 2 samples analysed. In fact, LTO-B is showing a higher resistivity (0.109 Ωcm) compared to LTO-A (0.066 Ωcm) (see Table 1) and this affects the electrochemical behaviour in particular at higher C-rates.

In addition, some differences between LTO-A and LTO-B are evidenced probably due also to some difficulties in the cell assembly with lab-made sensors.
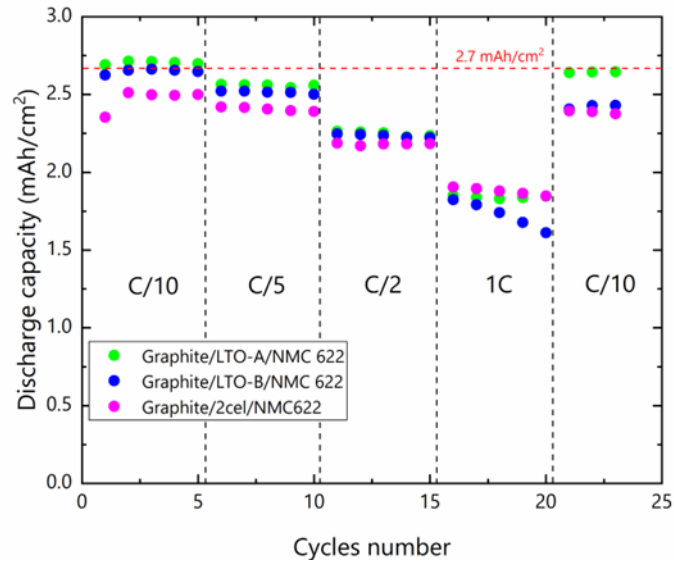

Figure 23. Discharge capacity of complete cells at different C-rates.

4.7 LTO sensor scale up and future work

To scale up the sensors production and to evaluate the capability to produce full cells closer to the possible commercial ones, six new samples have been sent by BDM to POL to perform EIS and evaluate the contribution of reference electrode. New configuration has been adopted by BDM printing the reference electrode onto a reduced area of the Celgard®2500 (Figure 26). This new sensor design can strongly reduce the mass of not active material in the cell, so increasing the overall energy density, and decreasing the overall cell resistance, so allowing to reach high C-rates.
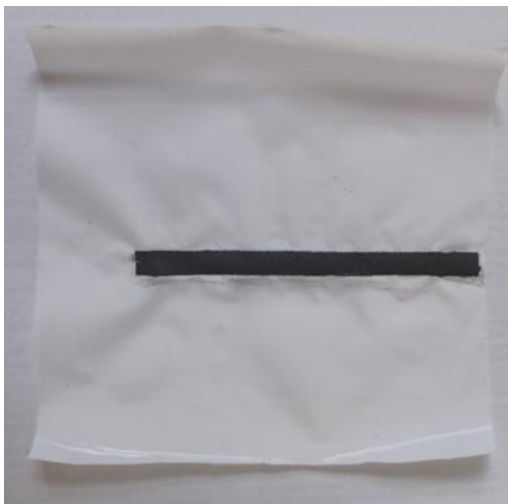

Figure 24. Example of new sample sent by BDM to POL.

Additional tests will be performed using the new smaller sensors produced by BDM to increase the Technology Readiness Level (TRL) of the produced sensors in the last period of the project.

5 Conclusions

This deliverable describes the activities of Task 2.4 regarding the characterization of the printed electrodes with different geometries, whose description has been reported in deliverable D2.2. The morphological and surface properties of the produced reference electrodes were characterised with several techniques, and afterward analysed electrochemically. After the optimization of the cell format, the impedance contribution of the printed reference electrodes within the cell was evaluated, indicating their suitability to perform electrochemical impedance spectroscopy (EIS) measurements in an extended frequency range (*i.e.*, frequency higher than 100 kHz), while marginally contributing to the series resistance of the cell. The functionalities of the printed reference electrodes for in situ/in operando sensing measurements of the battery electrodes was assessed by combining a full set of electrochemical analysis, including EIS, lithium plating/stripping, galvanostatic charge/discharge cycling, either using two- or three-electrode cell configurations. A preconditioning step of the sensors to bring them at a 50% state of charge (based on their nominal capacity) was found crucial to provide reliable and reproducible results.

The use of Lithium iron phosphate (LFP) and Lithium titanate (LTO) sensors as reference electrode was successfully demonstrated. We have tested the reference electrodes both structurally and electrochemically. The preliminary data indicated that the LTO-based electrode was the best performing one and therefore optimized in term of thickness and wettability. The optimized LTO-based reference electrode was then electrochemically characterized showing its capability to act as reference electrode in a full cell with NMC622 cathode and graphite anode.

Future activities will explore the integration of the reference electrode in the final 5 cm^2 pouch cell prototype, integrating the other sensing technology proposed by the project (Task 2.5).

6 Risks

Risk No.	What is the risk	Probability of risk occurrence[1]	Effect of risk[2]	Solutions to overcome the risk
1	*Difficulties in cell assembly*	*1*	*1*	*Improving the sealing/ encapsulation process*
2	*Impossible to test the assembled cells*	*1*	*1*	*Reassemble new cells*

---

[1] Probability risk will occur: 1 = high, 2 = medium, 3 = Low

[2] Effect when risk occurs: 1 = high, 2 = medium, 3 = Low

7 References

(1) B. Epding, A. Martin, B. Rumberg, H. Jahnke and A. Kwade, "Development of Durable 3-Electrode Lithium-Ion Pouch Cells with LTO Reference Mesh: Aging and Performance Studies," Journal of The Electrochemical Society, vol. 166, 2019.

(2) J. Liu, X. Wei and X.-W. Liu, *Sci. Rep.*, 2015, 5, 9782.

(3) P. Dhaiveegan, H.-T. Peng, M. Michalska, Y. Xiao, J.-Y. Lin and C.-K. Hsieh, *J. Solid State Electrochem.*, 2018, 22, 1851–1861.

(4) H. Beydaghi, S. Abouali, S. B. Thorat, A. E. Del Rio Castillo, S. Bellani, S. Lauciello, S. Gentiluomo, V. Pellegrini and F. Bonaccorso, *RSC Adv.*, 2021, 11, 35051–35060.

(5) S. Palumbo, L. Silvestri, A. Ansaldo, R. Brescia, F. Bonaccorso and V. Pellegrini, *ACS Appl. Energy Mater.*, 2019, 2, 1793–1802.

(6) H. Raj and A. Sil, *Ionics (Kiel).*, 2018, 24, 2543–2553.

(7) A. C. Ferrari and J. Robertson, *Phys. Rev. B*, 2000, 61, 14095–14107.

(8) A. C. Ferrari and J. Robertson, *Phys. Rev. B*, 2001, 64, 75414.

(9) A. C. Ferrari and D. M. Basko, *Nat. Nanotechnol.*, 2013, 8, 235–246.

(10) A. C. Ferrari, J. C. Meyer, V. Scardaci, C. Casiraghi, M. Lazzeri, F. Mauri, S. Piscanec, D. Jiang, K. S. Novoselov, S. Roth and A. K. Geim, *Phys. Rev. Lett.*, 2006, 97, 187401.

(11) J.-B. Wu, M.-L. Lin, X. Cong, H.-N. Liu and P.-H. Tan, *Chem. Soc. Rev.*, 2018, 47, 1822–1873.

(12) J. Ma, Q. Zhang, K. Lin, L. Zhou and Z. Ni, *Mater. Res. Express*, 2018, 5, 35057.

(13) A. Lakshmi-Narayana, M. Dhananjaya, N. Guru-Prakash, O. M. Hussain, A. Mauger and C. M. Julien, *ChemistrySelect*, 2018, 3, 9150–9158.

(14) J. Yang, J. Wang, D. Wang, X. Li, D. Geng, G. Liang, M. Gauthier, R. Li and X. Sun, *J. Power Sources*, 2012, 208, 340–344.

(15) S. Liu, P. Yan, H. Li, X. Zhang and W. Sun, *Front. Chem.*, , DOI:10.3389/fchem.2020.00104.

(16) M. Ender, J. Illig and E. Ivers-Tiffée, *J. Electrochem. Soc.*, 2016, 164, A71–A79.

(17) Z. Chu, X. Feng, B. Liaw, Y. Li, L. Lu, J. Li, X. Han and M. Ouyang, *J. Electrochem. Soc.*, 2018, 165, A3240–A3248.

(18) Y. Li, X. Han, X. Feng, Z. Chu, X. Gao, R. Li, J. Du, L. Lu and M. Ouyang, *J. Power Sources*, 2021, 481, 228933.

(19) Z. Zuo, L. Zhuang, J. :. S. Y. Xu, C. Su, P. Lian and B. Tian, " Lithiophilic Silver Coating on Lithium Metal Surface for Inhibiting Lithium Dendrites," Frontiers in Chemistry, vol. 8, 2020.

(20) X. Sun, P. Radovanovic and b. Cui, " Advances in Spinel Li4Ti5O12 Anode Material for Lithium-Ion Batteries," New J. Chem, vol. 39, 2014.

8 Acknowledgement

The author(s) would like to thank the partners in the project for their valuable comments on previous drafts and for performing the review.

Project partners

#	PARTICIPANT SHORT NAME	PARTNER ORGANISATION NAME	COUNTRY
1	IKE	IKERLAN S. COOP.	Spain
2	BDM	BEDIMENSIONAL SPA	Italy
3	POL	POLITECNICO DI TORINO	Italy
4	FHG	FRAUNHOFER GESELLSCHAFT ZUR FOERDERUNG DER ANGEWANDTEN FORSCHUNG E.V.	Germany
5	FM	FLANDERS MAKE VZW	Belgium
6	TUE	TECHNISCHE UNIVERSITEIT EINDHOVEN	The Netherlands
7	NXP NL	NXP SEMICONDUCTORS NETHERLANDS BV	The Netherlands
8	NXP FR	NXP SEMICONDUCTORS FRANCE SAS	France
9	ABEE	AVESTA BATTERY & ENERGY ENGINEERING	Belgium
10	VAR	VARTA MICRO INNOVATION GMBH	Germany
11	AIT	AIT AUSTRIAN INSTITUTE OF TECHNOLOGY GMBH	Austria
12	UNR	UNIRESEARCH BV	The Netherlands

DISCLAIMER/ ACKNOWLEDGMENT